Middle Eocene CO_2 and climate reconstructed from the sediment fill of a subarctic kimberlite maar, DOI:10.1130/G39002.1

A.P. Wolfe, A.V. Reyes, D.L. Royer, D.R. Greenwood, G. Doria, M. Gagen, P.A. Siver, J.A. Westgate

APPENDIX DR1 - METHODS

Geochronology

Exploration drill core BHP 99-01 was drilled by BHP Billiton Inc. in 1999 and archived at the Geological Survey of Canada (Calgary). Drilled at a 47° angle, the core captures ~50 vertical-equivalent meters of lacustrine sediment overlain by 32 m of peat (Fig. 1), together representing the progressive infilling of the maar basin.

Two rhyolitic tephra at 70.88 and 73.41 m vertical-equivalent core depth were dated by isothermal plateau (ITPFT) and diameter-corrected (DCFT) glass fission-track techniques, which both correct for post-depositional partial annealing of fission tracks in volcanic glass. With ITPFT, correction for partial track fading is made by heating the glass shards for 30 days at 150 °C, while DCFT uses a correction factor based on a comparison of the average diameters of the induced and spontaneous fission tracks (Sandhu and Westgate, 1995; Westgate, 1989; Westgate et al., 2013). Two DCFT dates and one ITPFT date for these tephra beds were reported by Doria et al. (2011), but analytical details were not provided. Here we provide one additional ITPFT date and full analytical details and results for the two tephra beds (Table DR1), yielding ages ranging from 36.88 ± 3.28 Ma to 39.37 ± 3.53 Ma at 1σ. Given the <10% errors associated with each age estimate, the glass fission-track dates suggest an age of ~38 Ma for the transition between lacustrine and peat facies. Slightly more precise constraining ages for the uppermost lacustrine mudstone facies can be obtained by calculating the weighted mean and error of the two corrected ages for each of the upper tephra (38.40 ± 2.50 Ma, 1σ) and lower tephra (36.98 ± 2.36 Ma, 1σ). These tephra beds are conformable and undeformed; the apparent age reversal cannot be explained by deformation, but rather is due to error at the 1σ level of ~10% typical of glass fission-track dating methods. The glass fission-track age of the internal standard (Huckleberry Ridge Tuff) is very close to its consensus $^{40}Ar/^{39}Ar$ age (Table DR1), providing strong support for the accuracy of the Giraffe tephra glass fission-track ages.

We analyzed in detail a 21 m section (vertical equivalent depth) of peat in core BHP 99-01 that captures the terrestrialization of the lake system. This interval contains nonpermineralized wood of *Metasequoia occidentalis* (Coniferae: Cupressaceae) identified by xylotemy (Visscher and Jagels, 2003), and unambiguous foliage belonging to the same taxon (Fig. DR1). On the basis of tephra glass fission-track geochronology, the maximum age of the analyzed sequence lies between 36-40 Ma. The duration of the full 21 m of analyzed section can be tentatively estimated at ~20,000 years, accepting accumulation rates for middle Eocene lignites in the order of 1 mm yr^{-1} and only moderate compaction (Kojima et al., 1998). The interval over which we estimate the mean climate state and attendant CO_2 concentrations spans 7 m of vertical equivalent thickness, or ~7,000 years of continuous deposition.

Pollen and mutual climate range analyses

For pollen analysis, 12 g of sediment was crushed and successively digested in 25% HCl, 70% HF, Schulze's solution ($KClO_3$ + HNO_3), and NaClO in a hot water bath. Neutralized slurries were floated in heavy liquid (ZnBr at 2.0 g cm^{-3}), sieved to isolate the 10-150 µm fraction, and stained with Safranin-O. Mounts for light microscopy were prepared from the 10-150 µm, 45-150 µm, 20-45 µm, and 10-20 µm fractions; at least 200 higher plant pollen grains were identified for each sampled core interval (Fig. DR2; Sweet, 2000).

The mutual climate range (MCR) method is based on the principle that all organisms have physiological climate tolerances that limit their natural distribution to areas where reproductive success is possible (Ballantyne et al., 2010; Thompson et al., 2012). All taxa present in a single plant

community therefore coexist within the common overlap of their range of tolerance. The MCR approach benefits from the redundancy of incorporating climate tolerances of multiple taxa, and is not biased by the relative frequency of occurrence of individual floristic elements. We used climate range data from the natural distributions of modern North American trees and shrubs identified as nearest living relatives (NLRs) at the rank of genus, supplemented with data from other regions for taxa no longer native in North America (Table DR2; Fang et al., 2011; Thompson et al., 1999, 2015).

MCR analysis identifies the range of a given climatic parameter for the set of identified NLRs of a fossil assemblage where they can coexist today; e.g., the minimum MAT_{max} and maximum MAT_{min} where all NLRs overlap. Many studies using MCR have used the midpoint of this range across all identified NLRs as the estimate of the likely past climatic condition associated with the assemblage (Thompson et al., 2012). The estimate is often given, however, with the range also expressed as a measure of the uncertainty of the estimate (e.g., Eldrett et al., 2009, 2014; Pross et al., 2012). The list of NLRs from the Giraffe assemblages (pollen for most taxa; foliage and wood for *Metasequoia*) used for MCR is given in the footnotes of Table DR2. We used the modern climate envelope for natural (*i.e.* not cultivated) populations of *Metasequoia glyptostroboides*, while recognizing that this may be narrower than actual tolerances of early Cenozoic congeners (Liu et al., 2007). Removing *M. glyptostroboides* from our analyses lowers the estimates of MAT, CMMT and WMMT by only 0.0 - 1.3 °C and by only 5 cm for MAP. We excluded *Ginkgo* on the grounds that natural populations of living *Ginkgo* potentially reflect a small fraction of its potential climate range (Tang et al., 2012). We do not adjust our NLR climate tolerance ranges to account for the possible acquisition of increased cold tolerance during progressive Cenozoic cooling, suggesting that reconstructed temperature parameters are likely conservative with respect to the magnitude of inferred warming. In common with other analyses of pollen NLR records (e.g., Eldrett et al., 2009, 2014; Kotthoff et al., 2014), the bisaccates *Picea* and *Pinus* were not included in the MCR analysis. These pollen types were present at <15% abundance for 15 of 16 samples, consistent with these grains being transported great distances and so potentially not reflecting local vegetation (Davis and Webb, 1975). Were megafossils present, these taxa would have been included (e.g., Ballantyne et al., 2010).

Thompson et al. (2012) demonstrated for modern North American pollen spectra that the MCR method yielded temperature estimates that matched actual site values with small anomalies (e.g., anomalies for MAT and CMMT ± 0.8–2.2 °C, WMMT ± 0.3–1.8 °C) for broadleaf deciduous forest and mesic conifer forest of the west and east coasts of North America. However, boreal forest and tundra vegetation yielded poorer correspondences between observed and MCR estimated temperatures (MAT ± 2.7 & 4.7 °C respectively). In the test of MCR by Thompson et al. (2012), MAP estimates showed anomalies ± 108–285 mm versus observed values. As the Giraffe site paleovegetation is reconstructed as a mixed deciduous broadleaf-conifer forest, the results from the test of MCR by Thompson et al. (2012) lends confidence to our estimates.

The MCR technique has been rigorously tested for North American Neogene and extant samples for both accuracy and precision and is appropriate for Eocene pollen assemblages, yielding temperature estimates congruent with those from independent geochemical proxies (Eldrett et al., 2009, 2014; Pross et al., 2012). Because plant taxa can persist at their climatic extremes, with the potential of distorting the objectivity of reconstructions, Thompson et al. (2012) recommended an approach where equally 'weighted' values are applied from the 10th to 90th percentiles, and lower weights applied outside that range. However, we applied a bootstrap re-sampling technique to the pollen-based climate estimates in order to identify the highest probability estimates (Table DR2) for each stratigraphic level, consistent with recommendations to assess uncertainty for NLR-method proxies (Harbert and Nixon, 2015). All samples used in our analysis had at least 13 NLRs with climate range data (minimum: 13; maximum: 19; mean: 15 NLRs), in keeping with the recommendations of Thompson et al. (2012). Overall Giraffe locality paleoclimate estimates in the main text are calculated as the mean and standard deviation of the results from each stratigraphic level.

Wood cellulose and $\delta^{18}O$ analyses

We used a Wiley mill to grind pieces of Giraffe wood to <420 μm. α-cellulose was extracted from the ground samples using a modified Jayme-Wise method (Gaudinski et al., 2006), whereby samples were refluxed in 2:1 toluene:ethanol in a Soxhlet apparatus to remove resins and waxes, boiled in deionized water, delignified in $NaClO_2$ with glacial acetic acid, and washed in 17% NaOH to remove hemicellulose. We also leached Fe and Mn oxyhydroxides using hydroxylamine hydrochloride (H_3NO•HCl). The purity of α-cellulose was confirmed by electron microscopy and x-ray diffraction (Fig. DR3). Cellulose extracts were homogenized by sonication and freeze-dried prior to analysis for stable oxygen isotope ratios at Swansea University. Homogenized α-cellulose was weighed (~300 μg) into silver capsules and pyrolized in a Europa ANCA GSL elemental analyser interfaced by continuous flow to a Europa 20/20 gas-source isotope ratio mass spectrometer. Instrumental drift was monitored using multiple internal laboratory cellulose standards. All unknown samples were analyzed in duplicate (Fig. 2D), and reported values are the arithmetic mean of these analyses (Table DR3). α-cellulose oxygen isotope data are presented in standard δ-notation with respect to Vienna Standard Mean Ocean Water (VSMOW). Repeat analyses of laboratory standards indicate analytical precision of ~0.3‰.

We estimated the corresponding values of $\delta^{18}O$ for environmental waters accessed by the trees ($\delta^{18}O_{water}$) using the leaf-water model of Anderson et al. (2002):

$$\delta^{18}O_{water} \approx \delta^{18}O_{cellulose} - (1 - f) * (1 - h) * (\varepsilon_e + \varepsilon_k) - \varepsilon_{biochem}$$

where f is the fraction of leaf water not subject to evaporation; ε_e is the liquid-vapor equilibrium fractionation factor (9.8‰ at 20 °C; Manjoube, 1971); ε_k is the liquid-vapor kinetic fractionation (28‰); h is the relative humidity; and $\varepsilon_{biochem}$ is the biologic fractionation for sugar converting to cellulose (27 ‰). For each stratigraphic level, we solved the leaf-water model 1000 time, with fixed variables for ε_e, ε_k, and $\varepsilon_{biochem}$, and random resamples of normal distributions for h (0.7±0.05), f (0.38±0.05), and $\delta^{18}O_{cellulose}$ (mean of duplicate isotope analyses ± 0.3‰ analytical precision). The distributions for f and h capture ranges determined from, respectively, a transfer function based on contemporary observations of temperature and relative humidity (Anderson et al., 2002) and independent studies of Eocene climates in the Canadian Arctic (Eberle and Greenwood, 2012; Eldrett et al., 2009; Jahren, 2007). MAT was then calculated for the 1000 leaf-water model solutions for each stratigraphic level using the empirical relation between Eocene river water and MAT (Fricke and Wing, 2004), in order to capture the different latitudinal temperature gradient during the epoch:

$$\delta^{18}O_{water} = -0.01T^2 + T - 22.91$$

where T is MAT. Median and 16th and 84th percentile values were computed from the range of solutions for reconstructed MAT at each stratigraphic level (Fig. 2E). We determined an overall cellulose-derived MAT estimate for the Giraffe site by combining the distributions of MAT estimates from all seven stratigraphic levels and calculating a median MAT and associated 16.5% to 83.5% quantile range of 15.6 ± 2.0 °C (Fig. DR4).

CO_2 reconstructions

Stomatal index-based CO_2 estimates for the Giraffe peaty sediments are described fully in Doria et al. (2011). In brief, the stomatal index (SI; stomatal density/[stomatal density+epidermal cell density]×100) of many plant species responds inversely to CO_2 partial pressure (Royer, 2001). The response is underpinned by clear genetic, functional, and signaling pathways and is furthermore not strongly affected by environmental gradients in water availability and irradiance (Gray et al., 2000; Salisbury, 1927; Woodward and Bazzaz, 1988). We measured fossil *Metasequoia* leaf populations from ten discrete stratigraphic levels that preserved sufficient intact foliage. For each leaf, a leaf-mean SI was computed from five fields of view, and for each level a mean SI was computed from five leaf means. Corresponding atmospheric CO_2 concentrations were then calculated using the extensive calibration between CO_2 and SI in extant *Metasequoia* (Beerling et al., 2009), coupled to Monte Carlo

simulations to generate robust uncertainties (Table DR4) propagated from both fossil and modern calibration SI (Doria et al., 2011).

We also estimated CO_2 with a plant gas-exchange model that uses stomatal density, stomatal size, and leaf $\delta^{13}C$ as inputs (Table DR4; Franks et al., 2014; Maxbauer et al., 2014). In contrast to stomatal indices, the gas-exchange method does not require extant calibrations and can produce well-bounded CO_2 estimates even at high CO_2 (Table DR4). However, the stomatal density measurements for Giraffe material are based on stomata-bearing portions of the leaf only, rather than mean stomatal density across the leaf as required by the gas exchange model. We used a scalar developed for Axel Heiberg Island *Metasequoia* (Maxbauer et al., 2014) to correct the measured stomatal density by a factor of 0.29±0.0005 at 1σ, the fractional leaf surface area composed of stomatal zones. Photosynthetic rate and the ratio of operational to maximum conductance, which are also needed for the model, came from measurements on extant *Metasequoia occidentalis* (Maxbauer et al., 2014). Uncertainties in all model input terms are provided in Table DR4; uncertainties were fully propagated by Monte Carlo simulations (10,000 random samples of all input terms).

For both the SI and gas-exchange CO_2 reconstructions at the ten stratigraphic levels (Fig. 2F), we combined the estimates from Monte Carlo simulations into a site-level estimate ("SI" and "GE" in Fig. 3A). We did this for each proxy by randomly drawing 10,000 resamples from the associated level×reconstruction matrix. The sharp drop in probability above 1500 ppm for the SI-based estimates reflects the upper bound of the extant calibration (Doria et al., 2011), meaning that the probability of >1500 ppm CO_2 is low but not zero. Many of the individual-level estimates of CO_2 quantitatively exclude this possibility (Fig. 2F; Table DR4). To calculate a single, multi-proxy CO_2 estimate for the site ("CR" in Fig. 3A), we randomly drew 5000 resamples from each of the "SI" and "GE" distributions. For each of these combined estimates of CO_2 concentration, reported uncertainties around the median are given as the 16th to 84th percentile of the distribution, similar to a 68% or 1σ confidence interval.

Paleoclimate inferences

The proxy-based estimate of Giraffe MAT was compared to results from an ensemble of Eocene climate simulations (Lunt et al., 2012) by calculating Giraffe-region MATs from the array of model grid cells spanning 65 °N, 108.75 °W to 60 °N, 78.75 °W (Table DR5), in order to incorporate paleogeographic uncertainties. Regional climate sensitivity specific to the Giraffe locality was calculated following Equation 3 of Royer et al. (2012):

$$\text{climate sensitivity} = \Delta MAT / (CO_{2;double} + \Delta S + \Delta T_{geo})$$

where ΔMAT is relative to present-day Yellowknife, $CO_{2;double}$ is reconstructed CO_2 expressed as units of CO_2 doubling relative to preindustrial, ΔS is a correction for lower Eocene solar luminosity, and ΔT_{geo} is a paleogeography correction factor. In a Monte Carlo simulation, we resampled 10,000 times from each of the SI, gas-exchange, and combined CO_2 distributions and the pollen MCR MAT normal distribution of 14.5±1.3 °C. These resamples were recast, respectively, to units of CO_2 doubling relative to pre-industrial and ΔMAT relative to present-day Yellowknife, where a doubling of CO_2 has a forcing of +3.7 W/m^2 (Myhre et al., 1998). This calculation was corrected for the radiative effects of both slightly lower middle Eocene solar luminosity (-0.215 units of CO_2 doubling, or -0.79 W/m^2 at 38 Ma relative to the present-day; Gough, 1981) and Eocene paleogeography (see below), and is equivalent to a regional $S_{[CO2,GEO]}$ following the syntax of Rohling et al. (2012). We made these corrections because the radiative forcings related to changes in luminosity and paleogeography are unrelated to the CO_2 radiative response; for our calculations, we assume that all other changes in radiative forcing are a feedback response to the change in CO_2 (e.g., other well-mixed greenhouse gases such as methane).

There is currently insufficient knowledge of regional paleogeography and climate boundary conditions to apply a precise paleogeography correction. Instead, we parameterize this effect with 10,000 resamples drawn from a normal distribution of +0.50 ± 0.25 units of CO_2 doubling relative to pre-industrial (+1.85 ± 0.93 W/m^2). In this strategy, the generated paleogeographic effect is higher than most estimates of the mean global effect (Royer et al., 2012), which has the net effect of producing conservative, even underestimated, values of ESS. When the paleogeography correction is removed, regional climate sensitivity for the Giraffe locality increases by 2.4 °C per CO_2 doubling. Given age model limitations, it is not possible to apply an orbital forcing correction factor for MAT; the estimated duration of deposition for the full 21 m sampled interval spans most of a precessional cycle and half an obliquity cycle.

Probability density functions for plotting the resampled CO_2 reconstructions and regional climate sensitivity were generated using the R software package *density* routine for kernel density estimation, with a Gaussian kernel and default smoothing bandwidth.

APPENDIX DR1 REFERENCES CITED

Anderson, W.T., Bernasconi, S.M., McKenzie, J.A., Saurer, M., and Schweingruber, F., 2002, Model evaluation for reconstructing the oxygen isotopic composition in precipitation from tree ring cellulose over the last century: Chemical Geology, v. 182, p. 121-137.

Ballantyne, A.P., Greenwood, D.R., Sinninghe Damsté, J.S., Csank, A.Z., Eberle, J.J., and Rybczynski, N., 2010, Significantly warmer Arctic surface temperatures during the Pliocene indicated by multiple independent proxies: Geology v. 38, p. 603-606.

Beerling, D.J., Fox, A., and Anderson, C.W., 2009, Quantitative uncertainty analyses of ancient atmospheric CO_2 estimates from fossil leaves: American Journal of Science, v. 309, p. 775–787.

Davis, R.B. and Webb III, T., 1975, The contemporary distribution of pollen in eastern North America: a comparison with the vegetation: Quaternary Research, v. 5, p. 395–434.

Doria, G., Royer, D.L., Wolfe, A.P., Fox, A., Westgate, J.A., and Beerling, D.J., 2011, Declining atmospheric CO_2 during the late Middle Eocene climate transition: American Journal of Science, v. 311, p. 63-75.

Eberle, J. J., and Greenwood, D. R., 2012, Life at the top of the greenhouse Eocene world - a review of the Eocene flora and vertebrate fauna from Canada's High Arctic: Geological Society of America Bulletin, v. 124, p. 3-23.

Eldrett, J.S., Greenwood, D.R., Harding, I.C., and Huber, M., 2009, Increased seasonality through the Eocene to Oligocene transition in northern high latitudes: Nature, v. 459, p. 969-974.

Eldrett, J.S., Greenwood, D.R., Polling, M., Brinkhuis, H., and Sluijs, A. 2014, A seasonality trigger for carbon injection at the Paleocene–Eocene Thermal Maximum: Climate of the Past, v. 10, pp. 759–769

Fang, J., Wang, Z., and Tang, Z., 2011, Atlas of woody plants in China: distribution and climate, vols. 1 and 2: Berlin, Springer-Verlag.

Franks, P.J., Royer, D.L., Beerling, D.J., Van de Water, P.K., Cantrill, D.J., Barbour, M.M., and Berry, J.A., 2014, New constraints on atmospheric CO_2 concentration for the Phanerozoic: Geophysical Research Letters, v. 41, p. 4685-4694.

Fricke, H.C., and Wing, S.L., 2004, Oxygen isotope and paleobotanical estimates of temperature and $\delta^{18}O$-latitude gradients over North America during the early Eocene: American Journal of Science, v. 304, p. 612-635.

Gansecki, C.A., Mahood, G.A., and McWilliams, M., 1998, New ages for the climactic eruptions of Yellowstone: single-crystal $^{40}Ar/^{39}Ar$ dating identifies contamination: Geology, v. 26, p. 343-346.

Gaudinski, J.B., et al., 2005, Comparative analysis of cellulose preparation techniques for use with 13C, 14C, and 18O isotopic measurements: Analytical Chemistry, v. 77, p. 7212-7224.

Gough, D.O., 1981, Solar interior structure and luminosity variations: Solar Physics, v. 74, p. 21-34.

Gray, J.E., et al., 2000, The HIC signalling pathway links CO_2 perception to stomatal development: Nature, v. 408, p. 713-716.
Harbert, R.S., and Nixon, K.C. 2015, Climate reconstruction analysis using coexistence likelihood estimation (CRACLE): A method for the estimation of climate using vegetation: American Journal of Botany, v. 102, pp. 1277–1289.
Jahren, A.H., 2007, The arctic forest of the middle Eocene: Annual Review of Earth and Planetary Sciences, v. 35, p. 509-540.
Kojima, S., Sweda, T., LePage, B.A., and Basinger, J.F., 1998, A new method to estimate accumulation rates of lignites in the Eocene Buchanan Lake Formation, Canadian Arctic: Palaeogeography, Palaeoclimatology, Palaeoecology, v. 141, p. 115-122.
Kotthoff, U., Greenwood, D.R., McCarthy, F.M.G., Müller-Navarra, K., Prader, S., and Hesselbo, S.P., 2014, Late Eocene to middle Miocene (33 to 13 million years ago) vegetation and climate development on the North American Atlantic Coastal Plain (IODP Expedition 313, Site M0027): Climate of the Past, v. 10, p.1523-1539.
Laurenzi, M.A., et al., 2007, New constraints on ages of glasses proposed as reference materials for fission-track dating: Geostandards and Geoanalytical Research, v. 31, p. 105-124.
Laurenzi, M.A., Bigazzi, G., Balestrieri, M.L., and Bouska, V., 2003, $^{40}Ar/^{39}Ar$ laser probe dating of the central European tektite-producing impact event: Meteoritics and Planetary Science, v. 38, p. 887-893.
Liu, Y.J., Arens, N.C., and Li, C.S., 2007, Range change in Metasequoia: relationship to palaeoclimate: Botanical Journal of the Linnean Society, v. 154, p. 115-127.
Lunt, D.J., et al., 2012, A model-data comparison for a multi-model ensemble of early Eocene atmosphere–ocean simulations: EoMIP: Climate of the Past, v. 8, p. 1717-1736.
Manjoube, M., 1971, Fractionnement en oxygène 18 et en deuterium entre l'eau et sa vapeur: Journal Chimie Physique, v. 68, p. 1423-1436.
Maxbauer, D.P., Royer, D.L., and LePage, B.A., 2014, High Arctic forests during the middle Eocene supported by moderate levels of atmospheric CO_2: Geology, v. 42, p. 1027-1030.
Myhre, G., Highwood, E.J., Shine, K.P., and Stordal, F., 1998, New estimates of radiative forcing due to well mixed greenhouse gases: Geophysical Research Letters, v. 25, p. 2715-2718.
Pross, J., et al, 2012, Persistent near-tropical warmth on the Antarctic continent during the early Eocene epoch: Nature, v. 488, p. 73-77.
Rohling, E.J., et al., Making sense of palaeoclimate sensitivity: Nature, v. 491, p. 683-691.
Royer, D.L., 2001, Stomatal density and stomatal index as indicators of paleoatmospheric CO_2 concentration: Review of Palaeobotany and Palynology, v. 114, p. 1-28.
Royer, D.L., Pagani, M., and Beerling, D.J., 2012, Geobiological constraints on Earth system sensitivity to CO_2 during the Cretaceous and Cenozoic: Geobiology, v. 4, p. 298-310.
Salisbury, E.J., 1927, On the causes and ecological significance of stomatal frequency, with special reference to the woodland flora: Philosophical Transactions of the Royal Society B, v. 216, p. 1-65.
Sandhu, A.S., and Westgate, J.A., 1995, The correlation between reduction in fission-track diameter and areal track density in volcanic glass shards and its application in dating tephra beds: Earth and Planetary Science Letters, v. 131, p. 289-299.
Sweet, A.R., 2000, Geological Survey of Canada Paleontological Report 4-ARS-2000 (Geological Survey of Canada, Calgary).
Tang, C.Q., et al., 2012, Evidence for the persistence of wild *Ginkgo biloba* (Ginkgoaceae) populations in the Dalou Mountains, southwestern China: American Journal of Botany, v. 99, p.1408-1414.
Thompson, R.S., Anderson, K.H., and Bartlein, P.J., 1999, Atlas of relations between climatic parameters and distributions of important trees and shrubs in North America: U.S. Geological Survey Professional Paper 1650 A&B.

Thompson, R.S., Anderson, K.H., Pelltier, R.T., Strickland, L.E., Bartlein, P.J., and Shafer, S.L., 2012, Quantitative estimation of climatic parameters from vegetation data in North America by the mutual climatic range technique: Quaternary Science Reviews, v. 51, p. 18-39.

Thompson, R.S., Anderson, K.H., Pelltier, R.T., Strickland, L.E., Shafer, S.L., Bartlein, P.J., and McFadden, A.K., 2015, Atlas of relations between climatic parameters and distributions of important trees and shrubs in North America - Revisions for all taxa from the United States and Canada and new taxa from the western United States: U.S. Geological Survey Professional Paper 1650-G.

Tipple, B.J., Meyers, S.R., and Pagani, M., 2010, Carbon isotope ratio of Cenozoic CO_2: a comparative evaluation of available geochemical proxies: Paleoceanography, v. 25, PA3202.

Visscher, G., and Jagels, R., 2003, Separation of Metasequoia and Glyptostrobus (Cupressaceae) based on wood anatomy: IAWA Journal, v. 24, p. 439-450.

Westgate, J.A., 1989, Isothermal plateau fission-track ages of hydrated glass shards from silicic tephra beds: Earth and Planetary Science Letters, v. 95, p. 226-234.

Westgate, J.A., Naeser, N.D., and Alloway, B., 2013, Fission-track dating, in Elias, S.A., and Mock, C.J., eds., Encyclopedia of Quaternary Science (2nd edition): Amsterdam, Elsevier, p. 643-662.

Woodward, F.I., and Bazzaz, F.A., 1988, The responses of stomatal density to CO_2 partial pressure: Journal of Experimental Botany, v. 39, p. 1771-1781.

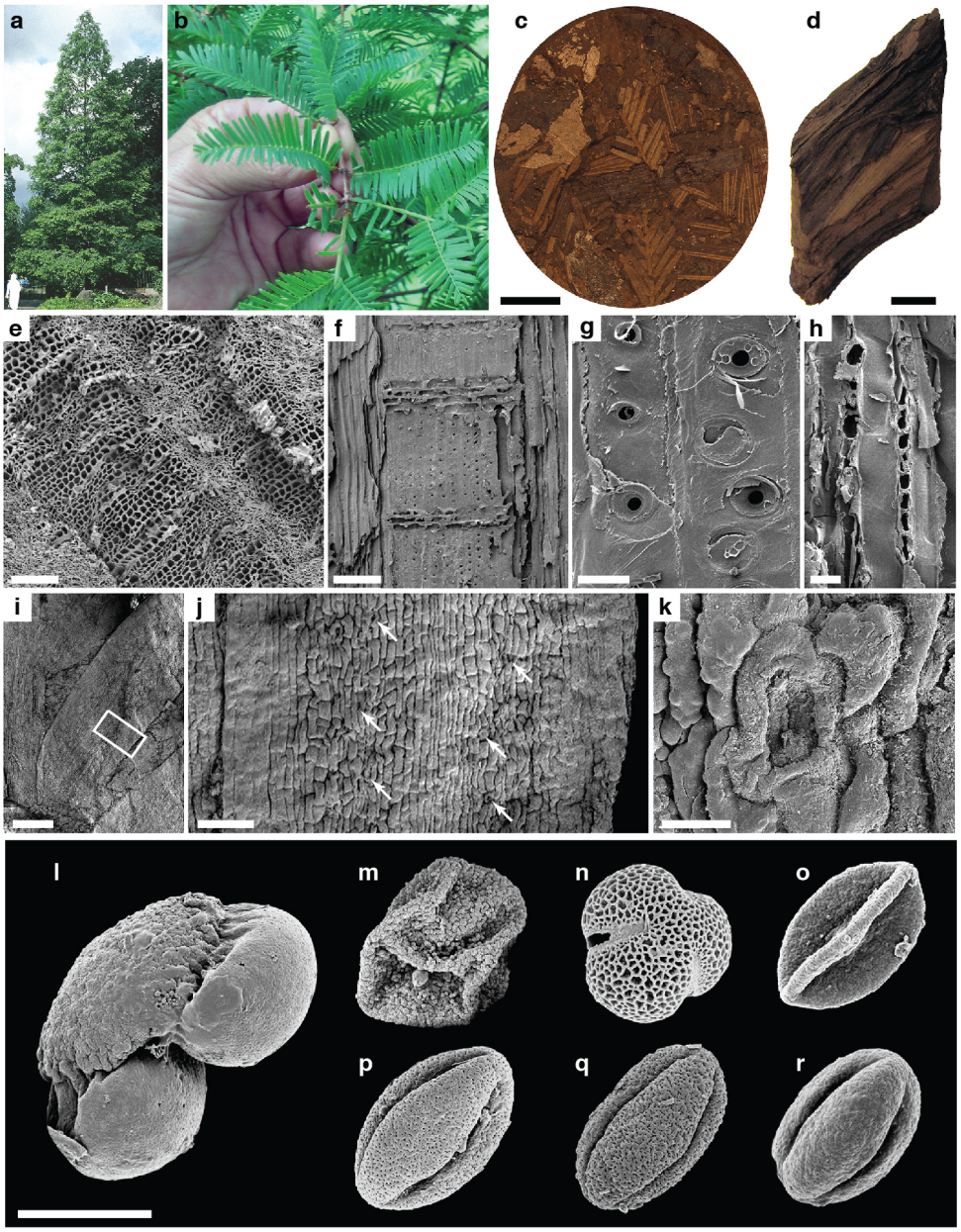

Figure DR1. Extant and fossil *Metasequoia* and assorted images demonstrating the quality of botanical preservation from the Giraffe kimberlite locality. (a, b) *Metasequoia glyptostroboides* from the Berlin arboretum. Specimen in (a) is ~20 m tall. (c) Litter-rich horizon in the Giraffe core, strongly dominated by *Metasequoia* foliage. (d) Wood fragment from the Giraffe core, showing preservation of shaggy cupressoid bark on the specimen surface. (e) Scanning electron microscopy (SEM) of unpermineralized wood in transverse section, revealing largely intact cell structure with only slight compression and the preservation of annual growth rings with diagnostic abrupt early- to late-wood transitions. (f) Bordered tracheid pits and rays in radial section under SEM. (g) Close-up of tracheid pits in radial section and (h), of uniseriate rays in tangential section. (i) SEM of individual leaf (abaxial surface). The white box is enlarged in (j), showing stomata (arrows) arranged in longitudinal rows. (k) Individual stoma under high-magnification SEM. (l) *Pinus* pollen grain. (m) *Metasequoia* pollen grain. (n) *Fraxinus* pollen grain. (o-r) Diverse fagalean palynomorphs. Scale bars are 1 cm (c, d); 1 mm (i); 100 µm (e, f, j); and 10 µm (g, h, k-r).

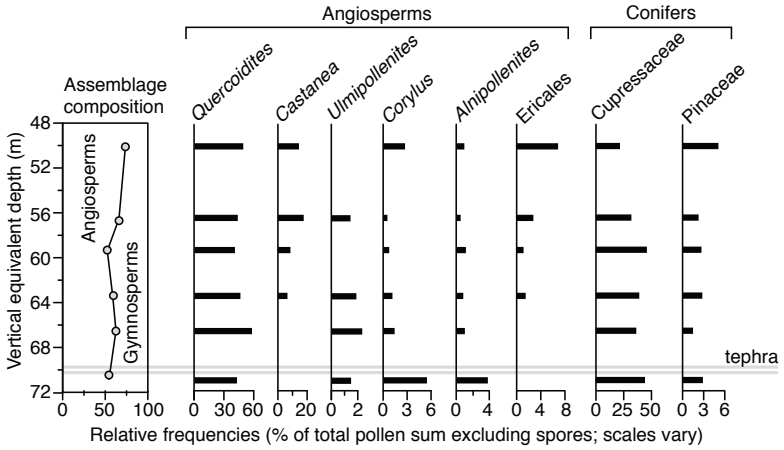

Figure DR2. Summary pollen diagram from the Giraffe peat section (data from Sweet, 2000).

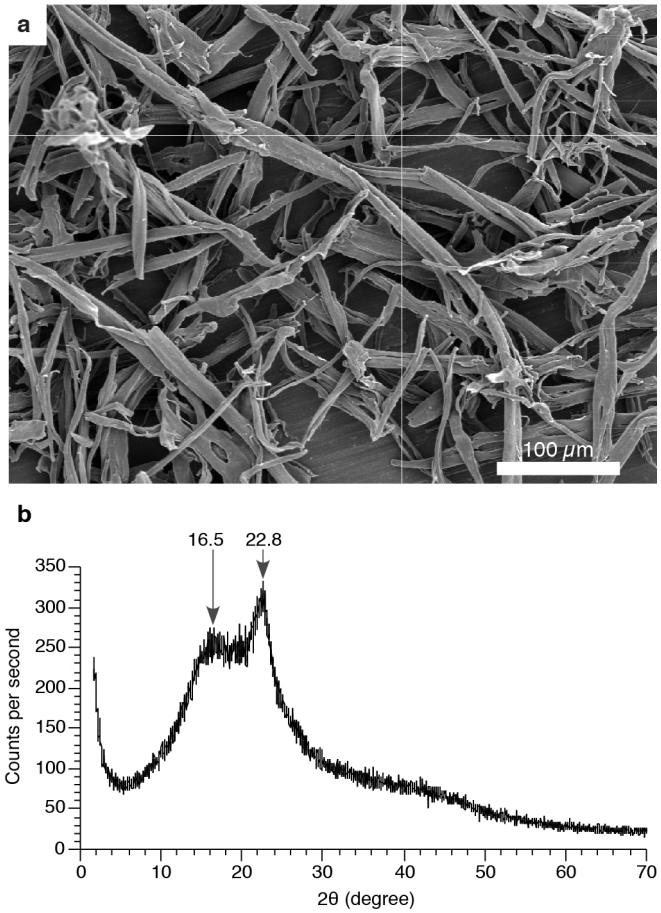

Figure DR3. Cellulose extracted from *Metasequoia* wood in the Giraffe kimberlite. a, Scanning electron micrograph of extracted cellulose showing the purity of the material. b, X-ray diffractogram of the same material, revealing the strong peaks at 16.5 and 22.8 degrees 2-θ that are associated with crystallinity of α-cellulose.

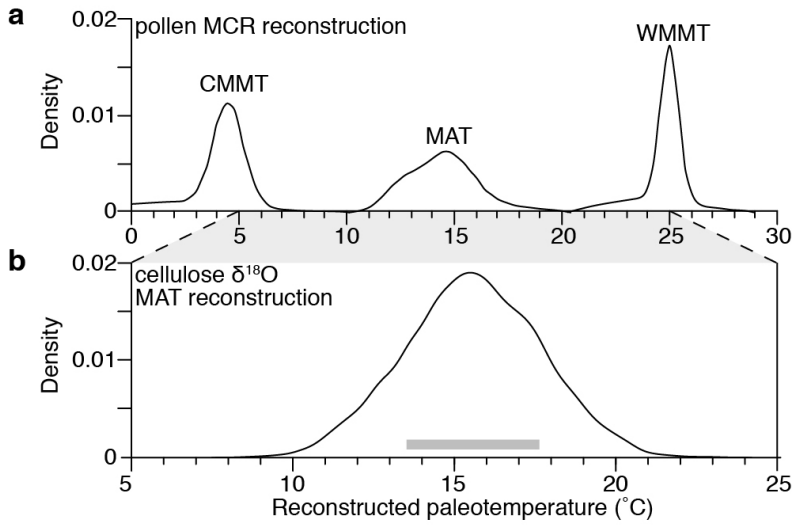

Figure DR4. Probability density functions for key climate parameters. a, coldest-month mean temperature (CMMT), mean annual temperature (MAT) and warmest-month mean temperature (WMMT) derived from pollen by the nearest living relative method, mutual climate range analysis (MCR). b, MAT derived from wood cellulose $\delta^{18}O$, with the 16th to 84th percentile indicated by the horizontal grey bar.

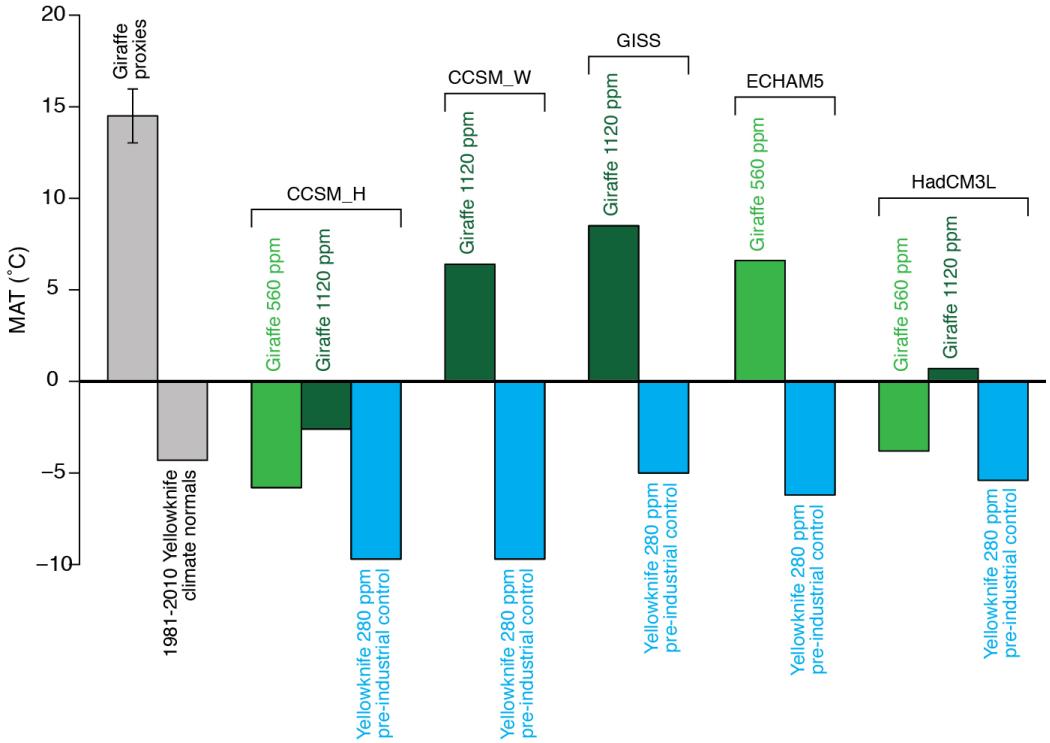

Figure DR5. Comparison of reconstructed (this study) and model results from various EoMIP simulations (Lunt et al., 2012) for MAT in the Giraffe region, relative to MAT for Yellowknife from 1981-2010 climate normals and the 280 ppm model control runs of Lunt et al. (2012). The corresponding ΔMAT for these models run at 560 and 1120 ppm CO_2 are plotted in Fig. 4 and tabulated in Table DR5.

Table DR1. Glass fission-track ages of tephra beds in the Giraffe kimberlite maar sediments.

Depth in core (m)	Vertical equivalent depth (m)	Method	Spontaneous track density (10^2 t/cm^2)	Corrected spontaneous track density (10^2 t/cm^2)	Induced track density (10^5 t/cm^2)	Track density on muscovite dosimeter glass (10^5 t/cm^2)	Etching conditions (HF %: ^{o}C: seconds)	D_s (μm)	D_i (μm)	D_s/D_i or D_i/D_s#	Age (Ma)
					UT2114 – Giraffe pipe tephra						
98.92	73.41	uncorrected	533.00 ± 6.13 (7557)		2.28 ± 0.01 (33653)	3.76 ± 0.04 (9567)	24: 24: 120	5.03 ± 0.06 [397]	6.56 ± 0.08 [596]	0.77 ± 0.01	26.39 ± 2.34
		DCFT		693.00 ± 7.97 (7557)	2.12 ± 0.01 (33653)	3.76 ± 0.04 (9567)	24: 24: 120	5.03 ± 0.06 [397]	6.56 ± 0.08 [596]	1.30 ± 0.02#	**36.88 ± 3.28****
		uncorrected*	409.00 ± 7.26 (3171)		1.73 ± 0.01 (61838)	3.75 ± 0.01 (14393)	24: 20.5: 130	5.03 ± 0.06 [397]	6.56 ± 0.08 [596]	0.77 ± 0.01	26.52 ± 2.44
		DCFT*		531.18 ± 9.43 (3171)	1.61 ± 0.01 (61838)	3.75 ± 0.01 (14393)	24: 20.5: 130	5.03 ± 0.06 [397]	6.56 ± 0.08 [596]	1.30 ± 0.02#	**37.08 ± 3.41**
					UT2115 – Giraffe pipe tephra						
96.39	70.88	uncorrected	502.00 ± 6.97 (5184)		2.04 ± 0.01 (32988)	3.81± 0.04 (9567)	24: 24: 125	5.62 ± 0.09 [199]	7.02 ± 0.10 [398]	0.8 ± 0.02	28.14 ± 2.67
		DCFT		627.00 ± 8.71 (5184)	1.91± 0.01 (2988)	3.81± 0.04 (9567)	24: 24: 125	5.62 ± 0.09 [199]	7.02 ± 0.10 [398]	1.25 ± 0.03#	**37.42 ± 3.55****
		ITPFT	455.00 ± 6.07 (5612)		1.32 ± 0.01 (23890)	3.81± 0.04 (9567)	24: 24: 180	6.47 ± 0.12 [199]	6.65 ± 0.08 [398]	0.97 ± 0.02	**39.37 ± 3.53****
					UT1366 – *Huckleberry Ridge tephra (internal standard)*						
		uncorrected	47.68 ± 4.06 (138)		3.19 ± 0.05 (4660)	3.67 ± 0.04 (9567)	24: 23: 120	5.77 ± 0.05 [611]	7.20 ± 0.08 [474]	0.80 ± 0.01	1.65 ± 0.14
		DCFT		59.60 ± 5.07 (138)	3.18 ± 0.05 (4660)	3.67 ± 0.04 (9567)	24: 23: 120	5.77 ± 0.05 [611]	7.20 ± 0.08 [474]	1.25 ± 0.02#	**2.07 ± 0.18**

Notes: t = tracks; HF = hydrofluoric acid; D_s = mean spontaneous track diameter; D_i = mean induced track diameter. Induced track density is calculated using the population-subtraction method (Laurenzi et al., 2007). Ages calculated using the zeta approach and $\lambda D = 1.551 \times 10^{-10} y^{-1}$. Zeta value is 301 ± 3 based on six irradiations at the McMaster Nuclear Reactor, Hamilton, Ontario, using the NIST SRM 612 glass dosimeter and the Moldavite tektite glass (Lhenice locality) with an $^{40}Ar/^{39}Ar$ plateau age of 14.34 ± 0.08 Ma (Laurenzi et al., 2003, 2007). Ages in bold font are those corrected for partial track fading, achieved by the diameter-corrected procedure (DCFT, Sandhu and Westgate, 1995) and the isothermal plateau method (ITPFT, Westgate, 1989). Area estimated using the point-counting method for UT 2114 and UT2115 and an eyepiece graticule for UT1366. Number of tracks counted is given in parentheses; number of tracks measured is given in brackets. The weighted mean ages and errors of corrected ages for UT2114 and UT2115 are 38.40 ± 2.50 Ma and 36.98 ± 2.36 Ma, respectively. The single-crystal (sanidine) laser-fusion $^{40}Ar/^{39}Ar$ age and 2σ error of Huckleberry Ridge tephra, the internal standard, is 2.003 ± 0.014 Ma (Gansecki et al., 1998). Note that UT2114* was irradiated at a different time to the other samples and the track-size data of UT2114 were used to calculate the age corrected for partial track fading. ** Indicates age determination first reported by Doria et al. (2011).

Table DR2. Palynological estimates of MAT, CMMT, and WMMT using the Mutual Climate Range technique (Thompson et al., 2012), and list of nearest living relative (NLR) taxa used in the analysis

Vertical equivalent depth (m)	MAT NLRs	MAT (˚C)	MAT error (˚C)	CMMT (˚C)	CMMT error (˚C)	WMMT (˚C)	WMMT error (˚C)	MAP (mm yr^{-1})	MAP error (mm yr^{-1})
50.13	14	12.5	3.2	0.5	3.5	23.5	1.8	1257	304
56.50	17	14.9	0.7	4.5	0.5	25.0	0.3	1257	304
59.35	14	14.9	0.7	4.5	0.5	25.0	0.3	1257	304
63.36	15	14.9	0.7	4.5	0.5	25.0	0.3	1257	304
66.37	13	16.3	0.7	4.5	0.5	25.0	0.3	1292	339
70.94	19	13.8	3.2	2.1	1.9	23.5	1.8	1257	304
Mean	**15**	**14.5**	**1.5**	**3.4**	**1.2**	**24.5**	**0.8**	**1263**	**310**
SD		**1.3**		**1.7**		**0.8**		**14**	

Note: MAT = mean annual temperature; NLR = nearest living relative; CMMT = coldest month mean temperature; WMMT = warmest month mean temperature; MAP = mean annual precipitation

NLRs used, all identified to modern genus from Giraffe pollen except where indicated; where only one species was available with climate range data, this is listed: *Metasequoia glyptostroboides* (from megafossils; the fossil taxon *M. occidentalis* is an anatomical match for the extant species *M. glyptostroboides*; modern genus is monotypic), *Thuja* spp., *Sciadopitys verticillata* (modern genus is monotypic), *Tsuga* spp., *Alnus* spp., *Castanea* spp., *Corylus* spp., *Quercus* spp., *Ulmus* spp., *Acer* spp., *Betula* spp., *Carya* spp., *Celtis* spp., *Cercidiphyllum japonica* (1 of 2 species with data), *Engelhardia* spp., *Eucommia ulmoides* (modern genus is monotypic), *Fagus* spp., *Fraxinus* spp., *Ilex* spp., *Juglans* spp., *Liquidambar styraciflua*, *Nyssa* spp., *Platycarya strobilacea* (modern genus is monotypic), *Pterocarya* spp., *Rhododendron* spp. (best match for pollen), *Rhus* spp., *Symplocos tinctoria* (one North American species with data), *Tilia* spp.

Table DR3. Oxygen stable isotopic results from cellulose extracted from Giraffe *Metasequoia* wood macrofossils.

Vertical equivalent depth (m)	$\delta^{18}O_{cell.}$ (‰ VSMOW)	Estimated $\delta^{18}O_{water}$ (‰ VSMOW)		Estimated MAT (˚C)	
		median	16th – 84th percentile	median	16th – 84th percentile
55.53	23.44 ± 0.07	-10.56	-11.9 - -9.3	14.4	12.6 - 16.2
56.28	24.28 ± 0.09	-9.68	-11.0 - -8.5	15.7	13.8 - 17.5
57.30	24.45 ± 0	-9.53	-10.9 - -8.3	15.9	13.9 - 17.8
57.69	24.7 ± 0.3	-9.26	-10.7 - -8.0	16.3	14.3 - 18.2
58.08	23.79 ± 0.09	-10.21	-11.5 - -9.0	14.9	13.1 - 16.7
59.68	24.46 ± 0.08	-9.50	-10.9 - -8.3	16.0	14.0 - 17.8
63.58	24.7 ± 0.04	-9.25	-10.7 - -8.1	16.3	14.3 - 18.1

Note: $\delta^{18}O_{cell}$ = $\delta^{18}O$ of α-cellulose, mean±stdev of duplicate isotope analyses; VSMOW = Vienna Standard Mean Ocean Water; MAT = mean annual temperature. $\delta^{18}O_{water}$ and MAT estimates are calculated following Anderson et al. (2002) and Fricke and Wing (2004).

Table DR4. Stomatal index and gas-exchange estimates of CO_2 from *Metasequoia* leaves from the Giraffe locality.

	SI				*gas-exchange-model reconstruction*					
Vertical equivalent depth (m)	stomatal index (%)	median CO_2 (ppm)	16th percentile (ppm)	84th percentile (ppm)	stomatal density (mm^{-2})	pore length (mm)	leaf $\delta^{13}C$ (‰)	median CO_2 (ppm)	16th percentile (ppm)	84th percentile (ppm)
58.16	9.85 (0.43)	440	353	592	57.6 (4.5)	29.0 (1.7)	-24.88	341	302	387
58.50	9.30 (0.29)	502	392	663	58.1 (4.5)	25.8 (2.0)	-26.18	425	373	489
58.73	8.77 (0.56)	761	487	1236	62.7 (4.7)	24.5 (2.5)	-26.74	452	393	525
59.20	9.40 (0.61)	544	392	894	65.9 (4.8)	25.1 (2.7)	-26.69	433	378	499
59.24	7.73 (0.73)	1072	749	1365	50.3 (4.2)	24.3 (2.7)	-26.81	521	448	616
60.00	9.59 (1.14)	746	429	1246	59.7 (3.1)	24.1 (0.8)				
62.06	8.59 (1.03)	860	509	1289	55.4 (4.4)	25.0 (1.3)	-26.82	483	422	561
64.46	8.97 (0.55)	673	446	1144	53.6 (4.3)	27.7 (2.8)	-26.42	440	383	510
65.69	8.92 (0.89)	778	472	1252	74.2 (5.1)	26.7 (3.7)	-28.47	522	447	615
65.70	8.95 (1.23)	799	476	1250	61.8 (4.6)	24.3 (4.5)	-24.58	352	303	417
Overall Giraffe locality	**9.01 (0.59)**	**634**	**433**	**1124**	**60.0 (7.2)**	**25.8 (1.7)**	**-26.40 (1.15)**	**432**	**353**	**538**

Notes: Values in parentheses are the measured ±1 s.e.m. Only one leaf per horizon was measured for $\delta^{13}C$; for these inputs, a one standard deviation uncertainty of ±0.2‰ was assumed. The following values and uncertainties for the gas-exchange model were assumed constant across all horizons (see Maxbauer et al. [2014] and Franks et al. [2014] for justification and Franks et al. [2014] for scripts to make CO_2 estimates): $\delta^{13}C$ of paleo-atmosphere: -6 ± 0.7 ‰ (based on the model of Tipple et al. [2010]); photosynthetic rate (A_0) at a set CO_2 value (CO_{2_0}): 6.67 ± 0.39 mmol m^{-2} s^{-1} at 396 ppm CO_2; leaf boundary layer conductance to CO_2 (g_{cb}): 2 ± 0.1 mol m^{-2} s^{-1}; scaling from photosynthetic rate (A) to leaf mesophyll conductance to CO_2 (g_m): 0.013 ± 0.00065 mol $mmol^{-1}$; scaling from pore length to single guard cell width: 0.70 ± 0.01; scaling from single guard cell width to stomatal depth: 1 ± 0.05; scaling from the area of a circle with the diameter of pore length to maximum stomatal pore area (a_{max}): 0.5 ± 0.025; scaling from maximum leaf conductance to CO_2 (g_{cmax}) to operational leaf conductance to CO_2 (g_{cop}): 0.34 ± 0.038. Overall Giraffe locality values are arithmetic mean for stomatal index, stomatal density, pore length, and leaf $\delta^{13}C$, and calculated from Monte Carlo simulations for SI and gas-exchange CO_2 reconstructions.

Table DR5. Eocene Modelling Intercomparison Project (EoMIP; Lunt et al., 2012) estimates of MAT (ºC) for the grid cells of the Giraffe region and ΔMAT relative to modern and modeled Yellowknife MAT.

		560 ppm			1120 ppm			Giraffe proxies
Model	$MAT_{Yellowknife\_280ppm}$	$MAT_{Giraffe\_Eocene}$	ΔMAT_{280ppm}	ΔMAT_{modern}	$MAT_{Giraffe\_Eocene}$	ΔMAT_{280ppm}	ΔMAT_{modern}	ΔMAT_{modern}
HadCM3L	-5.4	-3.8 ± 2.2	1.6	0.5	0.7 ± 2.3	6.1	5.0	-
ECHAM5	-6.2	6.6 ± 2.7	12.8	10.9	-	-	-	-
GISS	-5.0	-	-	-	8.5 ± 2.1	13.5	12.8	-
CCSM_W	-9.7	-	-	-	6.4 ± 1.6	16.1	10.7	-
CCSM_H	-9.7	-5.8 ± 4.23	3.9	-1.5	-2.6 ± 3.3	7.1	1.7	-
Giraffe proxies	-	-	-	-	-	-	-	18.8

Notes: $MAT_{Yellowknife\_280ppm}$ is the modelled MAT for the Yellowknife grid cell in control runs at 280 ppm CO_2; $MAT_{Giraffe\_Eocene}$ is the modeled early Eocene MAT for the array of 27 grid cells corresponding to the Giraffe locality; ΔMAT_{modern} and ΔMAT_{Eocene} are expressed relative to Yellowknife 280 ppm CO_2 control runs and modern instrumental MAT, respectively.